

First-order Raman spectra of double perovskites $\text{AB}'_{1/2}\text{B}''_{1/2}\text{O}_3$

S. A. Prosandeev^{1,2}, U. Waghmare³, I. Levin¹, and J. Maslar¹

¹*National Institute of Standards and Technology,
Gaithersburg, Maryland 20899-8520*

²*Physics Department, Rostov State University,
5 Zorge St., 344090 Rostov on Don, Russia*

³*Theoretical Sciences Unit J Nehru Centre for Advanced Scientific Research,
Jakkur PO, Bangalore 560 064, INDIA*

(Dated: March 22, 2022)

Abstract

First principles computations of Raman intensities were performed for perovskite-family compound $\text{CaAl}_{1/2}\text{Nb}_{1/2}\text{O}_3$ (CAN). This compound features 1:1 (NaCl-type) ordering of Al and Nb superimposed onto the $b^-b^-c^+$ octahedral tilting. Raman tensor for CAN was computed using the package for first-principles computations ABINIT (URL <http://www.abinit.org>). Computations performed for both untilted cubic ($Fm\bar{3}m$) and tilted monoclinic ($P2_1/n$) CAN structures showed that the strongest Raman lines are associated with the ordering of Al and Nb. The computed spectrum agreed qualitatively with the experimental data measured on powder (CAN is available in polycrystalline form only). The effect of cation disorder on the Raman intensities was considered using phenomenological theory of light scattering in the vicinity of a phase transition. We suggest that, for certain modes, the corresponding Raman intensities depend primarily on the average long range order while, for other modes, the intensities are determined by fluctuations of the order parameter.

I. INTRODUCTION

Electronic properties of double perovskites $AB'_{1/2}B''_{1/2}O_3$ are strongly influenced by the degree of B-cation ordering.^{1,2,3} Raman spectroscopy is an attractive technique for probing B-site ordering in perovskites.⁴ Raman spectra proved to be sensitive even to small nanoscale ordered regions. For example, Raman spectra of largely disordered $PbSc_{1/2}Ta_{1/2}O_3$ still feature well detectable lines attributed to the existence of nanoscale ordered regions.⁵

The quantitative theoretical description for Raman spectra of disordered or partially ordered double perovskites has not been developed. Furthermore, no first-principles computations of Raman intensities in completely ordered double perovskites have been reported. This lack of theoretical analyses of Raman intensities impedes development of Raman spectroscopy into a quantitative tool for probing B-cation ordering in perovskites.

Raman effect refers to a light scattering by normal vibrations having appropriate symmetry. Landau and Placzek⁶ have shown that Raman intensities can be expressed over the phonon-mediated change of high-frequency (electronic) dielectric permittivity $\varepsilon(\omega_L)$ where ω_L is the incident light frequency of a laser. The theory commonly exploits this relation to evaluate the effect of a specific vibration on Raman spectra. This approach requires complex computations of the high-frequency (electronic) dielectric permittivity tensor and its weak variations caused by ionic vibrations. First-principles computations of Raman spectra have been limited to several semiconductors (Si, Ge, SiO_2 etc.) and rare-earth transition-metal borocarbides.^{7,8,9,10,11)}

The present study reports the first attempt to compute Raman intensities for double perovskites from first principles. The paper is structurally as follows. Section 2 describes the general theory for the computation of Raman intensities. Section 3 considers ordered double perovskites $AB'_{1/2}B''_{1/2}O_3$ and includes three parts: the general theory of Raman spectra for cubic double perovskites (Section 3.1), results of the computations for the untilted cubic $CaAl_{1/2}Nb_{1/2}O_3$ (CAN) (Section 3.2), and results of the computations for the tilted monoclinic CAN (Section 3.3). The effect of B-cation disorder on the Raman spectra of double perovskites will be described in Section 4. Section 5 considers the effect of phonon dispersion on the Raman line profile. Finally, Section 6 summarizes the results obtained.

II. THEORY

Born and Huang¹² derived an expression, which reduces the computation of integral Raman intensities to the evaluation of the imaginary part of linear (Raman) susceptibility (we consider the part of this intensity connected with the mode i , polarization directed along α , and the field along β):

$$I_{i\alpha\beta} = \kappa R_{i\alpha\beta}^2 \int_{-\infty}^{\infty} [n(\omega) + 1] \text{Im} \chi_{i\alpha\beta}(\omega) d\omega \quad (1)$$

where $\kappa = 2\hbar(\omega_L - \omega_i)^4 / (\pi c^4)$, ω_L is the laser frequency, $R_{i\alpha\beta}$ is Raman tensor, $n(\omega) + 1 = [1 - \exp(-\hbar\omega/k_B T)]^{-1}$ is Bose occupation number, ω_i is the frequency of mode i , k_B is Boltzmann constant, \hbar is Planck constant, T is temperature, and $\chi_{i\alpha\beta}$ is the contribution of mode i to dielectric susceptibility. Kramers-Kronig transformation yields¹³:

$$I_{i\alpha\beta} = \frac{2\hbar(\omega_L - \omega_i)^4}{c^4 m_i \omega_i} [n(\omega_i) + 1] (R_{i\alpha\beta})^2 \quad (2)$$

Thus, the relative intensity of the Raman active modes is determined by the fundamental characteristics of the lattice dynamics: phonon frequency, mass, and Raman tensor.

The Raman tensor is a derivative of the electronic part of the dielectric permittivity tensor $\varepsilon_{\alpha\beta}$ at a laser frequency with respect to the i -th normal mode displacement:

$$R_{i\alpha\beta} = \frac{\partial \varepsilon_{\alpha\beta}(\omega_L)}{\partial Q_i} \quad (3)$$

The first-order Raman scattering can be described using the expansion of polarization

$$\begin{aligned} P_\alpha &= P_{\alpha 0} + \varepsilon_0 \sum_i R_{i\alpha\beta} E_\beta Q_i = \\ &= P_{\alpha 0} + \varepsilon_0 \sum_{n\gamma} m_i^{1/2} R_{i\alpha\beta, n\gamma} E_\beta e_{in\gamma} m_n^{-1/2} Q_i \end{aligned} \quad (4)$$

where $e_{m\gamma}$ is the eigenvector of a dynamical matrix, m_n is the mass of the atom n , and Q_i is the normal mode displacement magnitude. From Eq. (4):

$$R_{i\alpha\beta} = m_i^{1/2} \sum_{n\gamma} R_{\alpha\beta, n\gamma} e_{in\gamma} m_n^{-1/2} \quad (5)$$

Eq. (5) can be used to estimate the contribution of different ions in mode i into the Raman tensor.

The integral Raman intensity can be expressed as:

$$I_{i\alpha\beta} = \frac{2\hbar (\omega_L - \omega_i)^4}{m_0 c^4 \omega_i} [n(\omega_i) + 1] (r_{i\alpha\beta})^2 \quad (6)$$

with

$$r_{i\alpha\beta} = \left(\frac{m_i}{m_0} \right)^{-1/2} R_{i\alpha\beta} \quad (7)$$

where $m_0 = 1a.m.u.$

Expression (7) is applicable to single crystals. For powders, the integral intensity has be averaged over the possible directions of crystallites which can be accomplished using the rotation invariants

$$\begin{aligned} G_i^{(0)} &= \frac{1}{3} (r_{ixx} + r_{iyy} + r_{izz})^2 \\ G_i^{(1)} &= \frac{1}{2} [(r_{ixy} - r_{iyx})^2 + (r_{ixz} - r_{izx})^2 + \\ &\quad + (r_{izy} - r_{iyz})^2] \\ G_i^{(2)} &= \frac{1}{2} [(r_{ixy} + r_{iyx})^2 + (r_{ixz} + r_{izx})^2 + \\ &\quad + (r_{izy} + r_{iyz})^2] + \frac{1}{3} [(r_{ixx} - r_{iyy})^2 + \\ &\quad + (r_{ixx} - r_{izz})^2 + (r_{iyy} - r_{izz})^2] \end{aligned} \quad (8)$$

For the 90° and backscattering geometry, a (polarized) laser beam, and a scattered radiation analyzer in use, the (reduced) intensity for the powder can be expressed as^{6,14,15}:

$$\begin{aligned} I_{\parallel}^{powder} &\sim (\omega_L - \omega_i)^4 \frac{1+n(\omega_i)}{30\omega_i} \left[10G_i^{(0)} + 4G_i^{(2)} \right], \\ I_{\perp}^{powder} &\sim (\omega_L - \omega_i)^4 \frac{1+n(\omega_i)}{30\omega_i} \left[5G_i^{(1)} + 3G_i^{(2)} \right], \\ I_{tot}^{powder} &= I_{\parallel}^{powder} + I_{\perp}^{powder} \\ \rho_i^{powder} &= I_{\perp}^{powder} / I_{\parallel}^{powder} \end{aligned} \quad (9)$$

where subscripts \parallel and \perp correspond to the polarized and depolarized light, respectively.

Finally, one can plot the Raman spectrum by using the expressions:

$$\begin{aligned}
I_{||}^{powder}(\omega) &\sim \sum_i I_{i||}^{powder} \frac{\Gamma_i}{(\omega - \omega_i)^2 + \Gamma_i^2} \\
I_{\perp}^{powder}(\omega) &\sim \sum_i I_{i\perp}^{powder} \frac{\Gamma_i}{(\omega - \omega_i)^2 + \Gamma_i^2} \\
I_t^{powder}(\omega) &\sim \sum_i I_{it}^{powder} \frac{\Gamma_i}{(\omega - \omega_i)^2 + \Gamma_i^2}
\end{aligned} \tag{10}$$

where Γ_i is the damping constant for the i -th mode. The computation of this constant should be done separately. Here we concentrate on the computation of integral Raman intensities only.

III. RAMAN SPECTRA OF ORDERED $AB'_{1/2}B''_{1/2}O_3$ PEROVSKITES

A. Results of first-principles computations for cubic $CaAl_{0.5}Nb_{0.5}O_3$

$CaAl_{0.5}Nb_{0.5}O_3$ (CAN) crystallizes with a perovskite-like structure and exhibits 1:1 ordering of Al and Nb superimposed onto the $b^-b^-c^+$ tilting of oxygen octahedra.¹⁶ This combination of cation ordering and octahedral tilting yields monoclinic $P2_1/n$ symmetry with 20 atoms per unit cell.¹⁷ In the absence of tilting, the structure would adopt a cubic $Fm\bar{3}m$ symmetry yielding $A_{1g} + E_g + 2F_{2g}$ Raman-active modes (see Fig. 1 and Appendix). First-principles computations of vibration frequencies, dynamical charges, and infra-red spectra for the cubic and tilted monoclinic structures of CAN have been reported.¹⁶ The present study focuses on the computation of Raman intensities with the help of a package for *ab-initio* computations, ABINIT, which is a result of joint project between the Université Catholique de Louvain, Corning Incorporated, and other contributors.¹⁸ Ingredients needed for the calculation of responses to atomic displacements and homogeneous electric fields have been already described in the literature.^{19,20} We do not compute damping constants in the present study, only integral intensities. A damping constant $\Gamma_i = 10 \text{ cm}^{-1}$ was used for all modes.

First, we performed the first-principles computations for the 10-ion unit cell of CAN having symmetry $Fm\bar{3}m$ (no tilting). We used 8x8x8 Monkhorst-pack grid, ECUT=45 Ha and $\text{tolvrs} = \text{tolwfr} = 10^{-18}$. We computed high frequency (electronic) dielectric tensor for the 5 different normal mode displacements. Then, we interpolated the results with a polynomial and extracted the linear dependence of the high-frequency (electronic) dielectric permittivity on the normal mode displacement. The results of the computation of the Raman

tensors are summarized in Table 1. The A_{1g} mode has the largest Raman tensor. Table 2 presents the coefficients needed for the computation of the average Raman tensor for the F_{2g} modes. Results of the computation of Raman intensities are presented in Table 3 and Fig. 2.

B. Raman spectrum of tilted CAN structure ($P2_1/n$)

For the tilted CAN ($P2_1/n$), we used the eigenfrequencies and eigenvectors which are similar to those obtained by Cockayne.¹⁶ The lattice constants in these computations were taken from the experiment, but the distortion and the equilibrium atomic coordinates were determined selfconsistently under the constraint of a fixed volume. The obtained structure contains frozen tilting of the $b^-b^-c^+$ type in the Glazer notations, and the equilibrium structure is monoclinic $P2_1/n$ with the unit cell 4 times larger than the primitive perovskite cell. By using ABINIT, we computed high-frequency (electronic) dielectric tensor, $\varepsilon_{\alpha\beta}(\omega_L)$, for each of the displacements Q . In all cases, we used the same high precision and 8x8x8 Monkhorst-pack grid as in the computation for the cubic CAN. To facilitate the comparison with experiment, we used the damping constants of 8 cm^{-1} and 2 cm^{-1} at frequencies above and below 400 cm^{-1} , respectively.

Fig. 3 presents the experimental (a) and the calculated total (b), polarized (c), and depolarized (d) Raman spectra for a ceramic CAN (the integral intensities for all lines are shown in Table 5).

IV. DISORDERED $\text{AB}'_{1/2}\text{B}''_{1/2}\text{O}_3$ PEROVSKITES

Raman spectra of double perovskites reportedly are sensitive to the degree of cation order, η .⁵ The 1:1 order parameter for the $Pm\bar{3}m \rightarrow Fm\bar{3}m$ transition is a scalar and transforms according to the R_1^+ representation of the parent $Pm\bar{3}m$ space group. A useful insight into the dependence of Raman intensities on η can be obtained using phenomenological theories of light scattering in the vicinity of a phase transition.^{13,21} We start with the expression (7) and expand the Raman tensor into a series with respect to the order parameter:

$$r_{i\alpha\beta}(\mathbf{r}) = r_{i\alpha\beta,1}\eta(\mathbf{r}) + \dots \quad (11)$$

The change of dielectric permittivity $\varepsilon(\mathbf{r})$ is proportional to the product of $\eta(\mathbf{r})$ and displacement $Q(\mathbf{r})$. The Fourier transform of this product can be expressed as:

$$\Delta\varepsilon_q \sim \sum_{\mathbf{k}} \eta_{\mathbf{k}+\mathbf{q}} Q_{-\mathbf{k}} \quad (12)$$

Finally, the intensity of the light scattering is proportional to the statistical average of the square of $|\Delta\varepsilon_q|$:

$$I \sim \sum_{\mathbf{k}\mathbf{k}'} \langle \eta_{\mathbf{k}+\mathbf{q}} Q_{-\mathbf{k}} \eta_{-\mathbf{k}'-\mathbf{q}} Q_{\mathbf{k}'} \rangle \quad (13)$$

According to this expression, phonons in the entire Brillouin zone are excited if $|\eta| < 1$.

Recent experimental studies of η -dependence of Raman intensities in CAN have shown that the intensities corresponding to both F_{2g} - and E_g -related modes vary approximately as square of the order parameter.²² In contrast, the intensity of the A_{1g} line exhibited weak dependence on η . These observation can be understood by considering two particular cases of the general expression (13).

First, we consider the case when Q does not correlate with η :

$$I^{(1)} \sim \sum_{\mathbf{k}} \langle \eta_{\mathbf{k}+\mathbf{q}} \eta_{-\mathbf{k}-\mathbf{q}} \rangle \langle Q_{\mathbf{k}} Q_{-\mathbf{k}} \rangle \quad (14)$$

Now, we present $\eta(\mathbf{r})$ as the sum of the average order parameter, η_e and its fluctuation $\Delta\eta(\mathbf{r})$:

$$\begin{aligned} I^{(1)} &\sim \eta_e^2 \langle Q_{\mathbf{q}} Q_{-\mathbf{q}} \rangle + \\ &+ \sum_{\mathbf{k}} \langle \Delta\eta_{\mathbf{k}+\mathbf{q}} \Delta\eta_{-\mathbf{k}-\mathbf{q}} \rangle \langle Q_{\mathbf{k}} Q_{-\mathbf{k}} \rangle \end{aligned} \quad (15)$$

The second term is finite only in the vicinity of the phase transition temperature, and it is finite even above T_c (the $\mathbf{k} = 0$ contribution behaves²¹ as $|\tau|^{-1/2}$). The first term behaves as:

$$\eta_e^2 \sim \tau = \frac{T_c - T_a}{T_a} \quad (16)$$

where T_c is the order – disorder phase transition temperature, T_a the annealing temperature (the equation can be applied to the samples quenched from T_a). This type of the dependence was experimentally observed for the F_{2g} and E_g related modes in CAN.²²

Now we consider the case when Q and η are strongly correlated and the displacements are modulated by the order parameter:

$$Q(\mathbf{r}) \sim \eta(\mathbf{r}) \quad (17)$$

In particular, the displacements change sign at the antiphase domain boundaries following the change in the sign of the order parameter. so that changing the sign of the order parameter has no effect on the Raman intensity. Even at the antiphase domain wall, where η varies linearly from -1 to 1 , one gets a finite contribution to the intensity. Relation (17) is realized only for those modes which transform similarly to the order parameter. In the symmetry group, $Fm\bar{3}m$, only the A_{1g} mode transforms similarly to $R1^+$ mode in $Pm\bar{3}m$.

In this case, (13) takes the form:

$$\begin{aligned} I_{it}^{(2)} = & C_i \eta_e^2 \langle \Delta \eta_{\mathbf{q}} \Delta \eta_{-\mathbf{q}} \rangle + D_i \eta_e^4 + \\ & + E_i \sum_{\kappa, \nu} \langle \Delta \eta_{\mathbf{q}+\kappa} \Delta \eta_{-\kappa} \Delta \eta_{-\mathbf{q}+\nu} \Delta \eta_{-\nu} \rangle + \\ & + F_i \eta_e \sum_{\kappa} \langle \Delta \eta_{\mathbf{q}+\kappa} \Delta \eta_{-\kappa} \Delta \eta_{-\mathbf{q}} \rangle \dots \end{aligned} \quad (18)$$

where²¹

$$\langle |\Delta \eta_{\mathbf{q}}|^2 \rangle \sim \tau^{-1} \quad (19)$$

The first term is temperature independent below T_c and should vanish above T_c . The second term is negligible in the vicinity of a phase transition (it varies as τ^2), and the last two terms are spread over phonon bands (they are finite above T_c). The third term depends²¹ on τ as $|\tau|^{-1/2}$. Experimental observations²² suggest that, the main contribution to light scattering for the A_{1g} mode comes from the first term in (39) and is temperature independent.

Thus, we conclude that the F_{2g} and E_g modes obey dependence (16) whereas A_{1g} mode shows mostly constant intensity below $T_a = T_c$. This difference stems from the fact that the A_{1g} mode transforms in the same way as the chemical order parameter while the F_{2g} and E_g modes transform differently.

The F_{2g} and E_g modes interact with strains, which can be constructed from the components of the gradient of the order parameter. This interaction mixes the polarized and depolarized spectra.

In the distorted (tilted) structure of CAN, there are Raman lines originating presumably

from tilting but not from the chemical ordering. A ferroelastic order parameter should supplement η , in this case.¹³

V. PHONON BAND WIDTH

Disorder can cause excitation of the q -points in the entire Brillouin zone.^{23,24,25,26} The contribution of this effect to the width of the Raman line is limited by the width of the corresponding phonon band. We have performed first-principles computation of phonon frequencies for a 80-ion cubic supercell of CAN (Viena DFT package VASP^{27,28} was used) and compared the results with those obtained for the tilted 20-ion supercell¹⁶ (Fig. 4). According to our results, the upper branch of the phonon bands (which includes the point corresponding to the A_{1g} mode) has the width of about 70 cm^{-1} , which is comparable to the width of the A_{1g} Raman line detected experimentally (about 40 cm^{-1}). Such narrow width increased only slightly with temperatures approaching T_c , which can be attributed to relatively narrow width of the corresponding phonon band. This relatively narrow width of the high frequency phonon bands in CAN can be caused by the band folding due to a doubling of the unit cell upon ordering.

VI. SUMMARY

We have performed *ab initio* computations of Raman intensities for the $\text{AB}'_{1/2}\text{B}''_{1/2}\text{O}_3$ perovskites. The computation of the Raman intensities in cubic CAN revealed that all Raman-active lines, $A_{1g}+E_g+2F_{2g}$, exhibit large relative intensities in single crystals. The low-frequency part of the Raman spectrum computed for the untilted cubic CAN structure differs significantly from the corresponding part of the Raman spectrum for the tilted monoclinic CAN. The intense lines in the cubic structure at 101 cm^{-1} shift to higher frequencies, split (188 cm^{-1} , 242 cm^{-1} , and 211 cm^{-1}),¹⁶ and become relatively weak. This is a result of the change in frequency, occupation number, and Raman tensor for this line. The high-frequency F_{2g} line in the cubic structure at 445 cm^{-1} splits in the low-symmetry structure into three lines at 446 cm^{-1} , 452 cm^{-1} and 457 cm^{-1} .¹⁶ The relative intensities of these lines decrease in the distorted structure though to a lesser extent than for the low-frequency F_{2g} line. E_g line at 660 cm^{-1} splits into two lines at 553 cm^{-1} and 554 cm^{-1} ,¹⁶ and the integral

intensity for this line decreases. A_{1g} line at 910 cm^{-1} in the cubic structure exhibits significant downshift to 797 cm^{-1} in the distorted CAN.¹⁶ Experimentally, this line is observed at higher frequency of 844 cm^{-1} . This discrepancy between the experimental and computed frequencies can be due to the overestimated degree of tilting in the DFT computations. The computed Raman intensities agree qualitatively with those observed experimentally. Yet, the experiment yields relative integral intensity of the A_{1g} line larger than the computed value (mostly due to the larger width), and the computed E_g intensity is smaller in the computation in comparison with experiment. This can be related to the contribution from the scattering on the powder surfaces. Second order Raman processes can contribute to the detected line intensity as well.

On the basis of the present first-principles computation we conclude that: (i) In agreement with earlier speculations,⁵ high-frequency Raman lines appear in $AB'_{1/2}B''_{1/2}O_3$ double perovskites mainly due the ordering of B' and B'' ions; (ii) The modulation of the ionic vibrations by the order parameter in CAN can explain the weak dependence of the A_{1g} line intensity in CAN on the annealing temperature when approaching T_c ; (iii) Our first-principles computation has shown that the width of the high-frequency phonon band is about 70 cm^{-1} that can explain the weak dependence of the high-frequency Raman lines asymmetry in CAN on the degree of disorder.

Acknowledgement

We are grateful to Arkady Levanyuk, Jan Petzelt, Oleksiy Svitelskiy, Sergey Vakhrushev, Eric Cockayne, Ronald Cohen, Andrew Rappe, Benjamin Burton and David Vanderbilt for stimulating discussions. S.A.P appreciates grants ru.01.01.037 (“Russian Universities”), 04-02-16103 (RFBR), and support from the NIST MSEL’s Director’s Reserve Fund. We express our appreciation to Xavier Gonze and Francois Detraux for their help with using ABINIT.

APPENDIX A: GENERAL EXPRESSIONS FOR CUBIC $Fm\bar{3}m$ STRUCTURE

Cubic $Fm\bar{3}m$ ordered perovskite $AB'_{1/2}B''_{1/2}O_3$ exhibits Raman active modes $A_{1g} + E_g + 2F_{2g}$. A_{1g} is a fully symmetric breathing vibration of oxygen octahedra (Fig. 1). The Raman tensor for this mode is diagonal,

$$r_{A_{1g}} = \begin{pmatrix} a & 0 & 0 \\ 0 & a & 0 \\ 0 & 0 & a \end{pmatrix}, \quad (\text{A1})$$

with the diagonal element

$$a = r_{A_{1g}zz} = (6m_O)^{-1/2} (r_{zz,O1z} - r_{zz,O2z} + r_{zz,O3x} - r_{zz,O4x} + r_{zz,O5y} - r_{zz,O6y}) \quad (\text{A2})$$

here the oxygen atoms in an octahedron are numbered from 1 to 6 (Fig. 1).

Symmetry of the lattice requires that:

$$\begin{aligned} r_{zz,O2z} &= -r_{zz,O1z} = r_{xx,O3x} = -r_{xx,O4x} = \\ &= r_{yy,O5y} = -r_{yy,O6y} \\ r_{zz,O3x} &= -r_{zz,O4x} = r_{zz,O5y} = -r_{zz,O6y} = \\ &= r_{xx,O1z} = -r_{xx,O2z} = r_{xx,O5y} = -r_{xx,O6y} = \\ &= r_{yy,O1z} = -r_{yy,O2z} = r_{yy,O3x} = -r_{yy,O4x} \end{aligned} \quad (\text{A3})$$

$$(\text{A4})$$

Hence, (A2) reduces to:

$$r_{A_{1g}zz} = 2\sqrt{\frac{m_0}{6m_O}} (r_{zz,O1z} + 2r_{zz,O3x}) \quad (\text{A5})$$

where m_O is the mass of an oxygen atom. Thus, the Raman tensor for this mode is determined by the two quantities describing the longitudinal and transverse changes of polarization with respect to atomic displacements.

E_g mode corresponds to another type of breathing of oxygen octahedra (Fig. 1). This mode is doubly degenerate. The corresponding Raman tensors can be represented as:

$$r_{E_g(1)} = \begin{pmatrix} -b & 0 & 0 \\ 0 & -b & 0 \\ 0 & 0 & 2b \end{pmatrix}, \quad r_{E_g(2)} = \begin{pmatrix} c & 0 & 0 \\ 0 & -c & 0 \\ 0 & 0 & 0 \end{pmatrix} \quad (\text{A6})$$

where

$$\begin{aligned}
b &= \frac{1}{2}r_{E_g(1)zz} = \frac{1}{4\sqrt{3}m_O}(2r_{zz,O1z} - 2r_{zz,O2z} - \\
&\quad -r_{zz,O3x} + r_{zz,O4x} - r_{zz,O5y} + r_{zz,O6y}) \\
c &= r_{E_g(2)zz} = \frac{1}{2\sqrt{m_O}}(r_{zz,O3x} - \\
&\quad -r_{zz,O4x} - r_{zz,O5y} + r_{zz,O6y})
\end{aligned} \tag{A7}$$

From the symmetry relations (A3):

$$\begin{aligned}
b &= \frac{1}{\sqrt{3}m_O}(r_{zz,O1z} - r_{zz,O3x}) \\
c &= \frac{1}{\sqrt{m_O}}(r_{zz,O1z} - r_{zz,O3x})
\end{aligned} \tag{A8}$$

Therefore, the Raman tensor for the E_g modes is controlled by the same two constants as the Raman tensor for the A_{1g} mode, and

$$c = \sqrt{3}b. \tag{A9}$$

F_{2g} modes are triply degenerate and contain contributions from the oxygen and A-cations. Oxygen-related F_{2gO} modes are presented in Fig. 1. Their Raman tensors are nondiagonal:

$$\begin{aligned}
r_{F_{2gO}(1)} &= \begin{pmatrix} 0 & d_O & 0 \\ d_O & 0 & 0 \\ 0 & 0 & 0 \end{pmatrix} \\
r_{F_{2gO}(2)} &= \begin{pmatrix} 0 & 0 & d_O \\ 0 & 0 & 0 \\ d_O & 0 & 0 \end{pmatrix} \\
r_{F_{2gO}(3)} &= \begin{pmatrix} 0 & 0 & 0 \\ 0 & 0 & d_O \\ 0 & d_O & 0 \end{pmatrix}
\end{aligned} \tag{A10}$$

where

$$d_O = r_{F_{2gO}(1),xy} = \frac{1}{2\sqrt{m_O}}(r_{xy,O3x} - r_{xy,O4x}) \tag{A11}$$

Because of the symmetry, only two ions out of six (those residing on axis x) contribute to this Raman tensor. The symmetry relations give:

$$\begin{aligned}
r_{xy,O3x} &= -r_{xy,O4x} = r_{xz,O3x} = \\
&= -r_{xz,O4x} = r_{yz,O5y} = -r_{yz,O6y} = \\
&= r_{yx,O5y} = -r_{yx,O6y} = r_{zx,O1z} = \\
&= -r_{zx,O2z} = r_{zy,O1z} = -r_{zy,O2z}
\end{aligned} \tag{A12}$$

Thus, only one constant determines the Raman tensors for the F_{2gO} modes:

$$d_O = \frac{1}{\sqrt{m_O}} r_{xy,O3x} \tag{A13}$$

The A-cation related (F_{2gA}) modes (Fig. 1) have the same Raman tensor as the oxygen related F_{2g} modes:

$$\begin{aligned}
r_{F_{2gA}(1)} &= \begin{pmatrix} 0 & d_A & 0 \\ d_A & 0 & 0 \\ 0 & 0 & 0 \end{pmatrix} \\
r_{F_{2gCa}(2)} &= \begin{pmatrix} 0 & 0 & d_A \\ 0 & 0 & 0 \\ d_A & 0 & 0 \end{pmatrix} \\
r_{F_{2gA}(3)} &= \begin{pmatrix} 0 & 0 & 0 \\ 0 & 0 & d_A \\ 0 & d_A & 0 \end{pmatrix}
\end{aligned} \tag{A14}$$

where

$$d_A = r_{F_{2gA}(1),xy} = \frac{1}{\sqrt{2m_A}} (r_{xy,A1z} - r_{xy,A2z}) \tag{A15}$$

with the symmetry relations:

$$\begin{aligned}
r_{xy,A1z} &= -r_{xy,A2z} = -r_{xz,a1y} = \\
&= r_{xz,A2y} = r_{yz,A1x} = \\
&= -r_{yz,A2x} = -r_{yx,A1z} = r_{yx,A2z} = \\
&= -r_{zx,A1y} = r_{zx,A2y}
\end{aligned} \tag{A16}$$

From these relations:

$$d_A = r_{F_{2g}A(1),xy} = \sqrt{\frac{2}{m_A}} r_{xy,A1z} \quad (\text{A17})$$

The eigenvectors of the F_{2g} modes are linear combinations of the O- and A-related normalized vectors:

$$e_{F_{2g}} = c_O e_{F_{2g}O} + c_A e_{F_{2g}A} \quad (\text{A18})$$

Their Raman tensors can be represented as linear combinations of the O- and A-related Raman tensors

$$r_{F_{2g}\alpha\beta} = c_O r_{F_{2g}O\alpha\beta} + c_A r_{F_{2g}A\alpha\beta} \quad (\text{A19})$$

The polarized $I_{i\parallel}^{cryst}$ and depolarized $I_{i\perp}^{cryst}$ Raman spectra of the cubic $AB_{1/2}B''_{1/2}O_3$ perovskites are determined by the diagonal and nondiagonal elements of the Raman tensor, respectively:

$$\begin{aligned} I_{i\parallel}^{cryst} &\sim (\omega_L - \omega_i)^4 \frac{r_{izz}^2}{\omega_i} [1 + n(\omega_i)] \\ I_{i\perp}^{cryst} &\sim (\omega_L - \omega_i)^4 \frac{r_{xxz}^2}{\omega_i} [1 + n(\omega_i)] \\ I_{it}^{cryst} &\sim I_{i\parallel}^{cryst} + I_{i\perp}^{cryst} \end{aligned} \quad (\text{A20})$$

From these quantities, the corresponding Raman spectra can be computed as:

$$\begin{aligned} I_{\parallel}^{cryst}(\omega) &\sim \sum_i I_{i\parallel}^{cryst} \frac{\Gamma_i}{(\omega - \omega_i)^2 + \Gamma_i^2} \\ I_{\perp}^{cryst}(\omega) &\sim \sum_i I_{i\perp}^{cryst} \frac{\Gamma_i}{(\omega - \omega_i)^2 + \Gamma_i^2} \\ I_t^{cryst}(\omega) &\sim \sum_i I_{it}^{cryst} \frac{\Gamma_i}{(\omega - \omega_i)^2 + \Gamma_i^2} \end{aligned} \quad (\text{A21})$$

The Raman spectra for powders can be found from expressions (10).

-
- ¹ G. A. Smolenskii, V. A. Bokov, V. A. Isupov, N. N. Krainik, R. E. Pasynkov, and A. I. Sokolov, *Ferroelectrics and related materials*, Gordon and Breach Sci. Publishers, N.Y., 1984.
- ² L. E. Cross, *Ferroelectrics* **76**, 241 (1987).
- ³ R. H. Mitchell, *Perovskites Modern and Ancient*, Almaz Press, Thunder Bay, 2002.
- ⁴ R. Loudon, *Adv. Phys.* **50**, 813 (2001).
- ⁵ I. G. Siny, R. S. Katiyar, and A. S. Bhalla, *Ferroel. Rev.* **2**, 51 (2000).

- ⁶ G. Placzek, in *Handbuch der Radiologie*, Vol. 6, Akademische Verlagsgesellschaft, Leipzig, 1934, p. 208.
- ⁷ S. Baroni and R. Resta, Phys. Rev. B **33**, 5969 (1986).
- ⁸ W. Windl, P. Pavone, K. Karck, O. Schütt, D. Strauch, P. Giannozzi, and S. Baroni, Phys. Rev. B **48**, 3164 (1993).
- ⁹ P. Umari, A. Pasquarello and A. Dal Corso, Phys. Rev. B **63**, 94305 (2001).
- ¹⁰ P. Umari and A. Pasquarello, J. Phys.: Condens. Matter **15**, S1547 (2000).
- ¹¹ P. Ravindran, A. Kjekshus, H. Fjellvåg, P. Puschnig, C. Ambrosch-Draxl, L. Nordström, and B. Johansson, Phys. Rev. B **67**, 104507 (2003).
- ¹² M. Born and K. Huang, Dynamical theory of crystal lattices, Oxford: Clarendon Press; New York: Oxford University Press, 1985.
- ¹³ J. Petzelt and V. Dvorák, J. Phys. C **9**, 1587 (1976).
- ¹⁴ W. Hayes and R. Loudon, Scattering of light by crystals, New York: Wiley, 1978, p. 113.
- ¹⁵ Hiro-o Hamaguchi, Adv. in Infrared and Raman Spectr. **12**, 273 (1985).
- ¹⁶ E. Cockayne, J. Appl. Phys. **90**, 1459 (2001).
- ¹⁷ I. Levin, J. Y. Chan, J. E. Maslar, T. A. Vanderah, and S. M. Bell, J. Appl. Phys. **90**, 904 (2001).
- ¹⁸ X. Gonze, J.-M. Beuken, R. Caracas, F. Detraux, M. Fuchs, G.-M. Rignanese, L. Sindic, M. Verstraete, G. Zerah, F. Jollet, M. Torrent, A. Roy, M. Mikami, Ph. Ghosez, J.-Y. Raty, and D. C. Allan, Computational Materials Science **25**, 478-492 (2002).
- ¹⁹ X. Gonze, Phys. Rev. B **55**, 10337 (1997).
- ²⁰ X. Gonze and C. Lee, Phys. Rev. B **55**, 10355 (1997).
- ²¹ V. L. Ginzburg, A. P. Levanyuk, and Sobyenin, Phys. Rep., **57**, 151 (1980).
- ²² I. Levin, S. Prosandeev, and J. Maslar, Appl. Phys. Lett. (submitted).
- ²³ Y. Yacoby, Z. Physik B **31**, 275 (1978).
- ²⁴ H. Richter, Z. P. Wang, and L. Ley, Solid State Commun. **39**, 625 (1981).
- ²⁵ M. Kitajima, Cryt, Rew. Sol. St. Mat. Sci. **22**, 275(1997).
- ²⁶ E. A. Rogacheva, Physica B **291**, 359 (2000).
- ²⁷ G. Kresse and J. Hafner, Phys. Rev. B **47**, 558 (1993).
- ²⁸ G. Kresse and J. Furthmüller, Phys. Rev. B **54**, 11169 (1996).
- ²⁹ A. D. Bruce, W. Taylor, and A. F. Murrrays, J. Phys. C **13**, 483 (1980).

TABLE I: Relative values of Raman tensor components obtained from the first-principles computations of cubic CAN.

notation	value
a	0.03084
b	0.00717
d _O	0.01572
d _{Ca}	0.00375

TABLE II: Eigenvectors for F_{2g} modes.

coefficients	F _{2g} I	F _{2g} II
c_O	0.9794	0.2019
c_{Ca}	-0.2019	0.9794

TABLE III: Relative intensities of Raman lines obtained in the first-principles computation for single crystal cubic CAN (T = 300K).

mode	ν [cm ⁻¹]	I^{cryst}	Geometry	I_t^{powder}	I_{\parallel}^{powder}	I_{\perp}^{powder}
A _{1g}	910	8.7388		8.7388	8.7388	0.0000
E _g	660	2.8332		1.6527	0.9444	0.7083
F _{2g} I	445	4.9791	⊥	6.9708	3.9833	2.9875
F _{2g} II	101	11.8411	⊥	16.5776	9.4729	7.1047

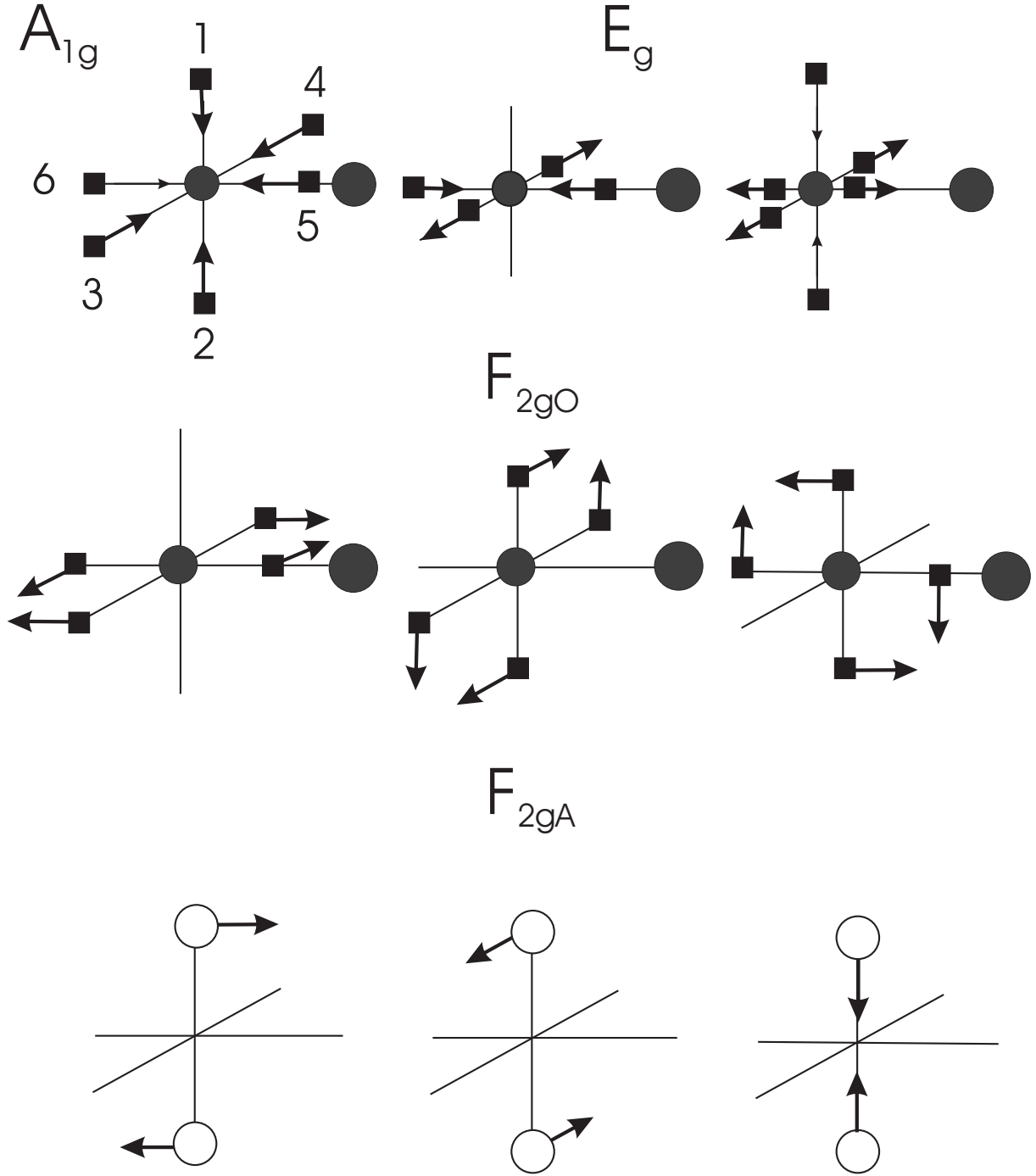


FIG. 1: The Raman active modes in $AB'_{1/2}B''_{1/2}O_3$ ordered perovskites ($Fm\bar{3}m$). Small and large filled circles denote ions B' and B'', filled squares are oxygens, and empty circles are ions A.

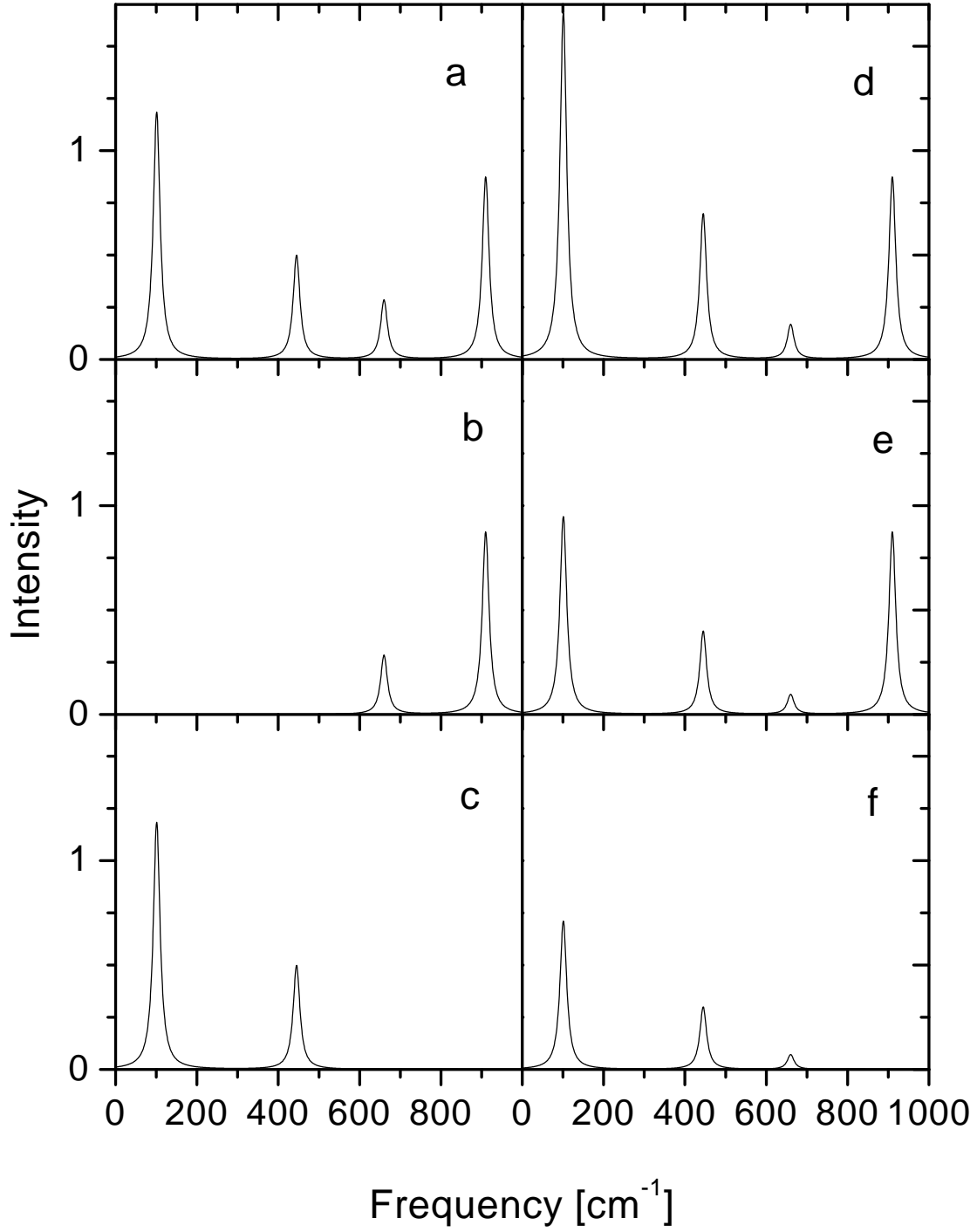


FIG. 2: Computed Raman spectrum of cubic CAN: I_t^{cryst} (a), $I_{||}^{cryst}$ (b), I_{\perp}^{cryst} (c), I_t^{powder} (d), $I_{||}^{powder}$ (e), I_{\perp}^{powder} (f).

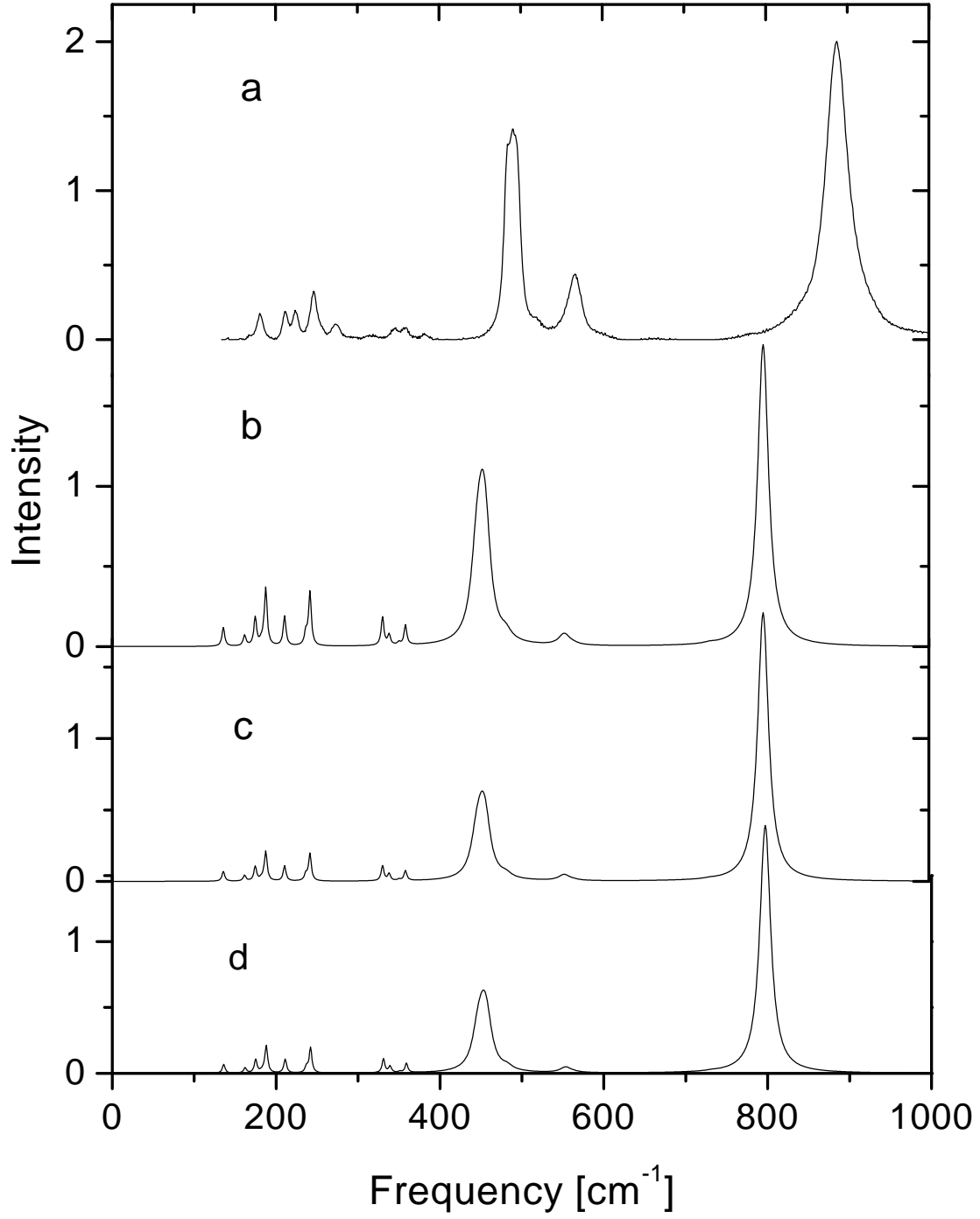


FIG. 3: Computed Raman intensities for ceramic CAN ($P2_1/n$): experiment^{17,22} (a), theory: I_t^{powder} (b), I_{\parallel}^{powder} (c), I_{\perp}^{powder} (d).

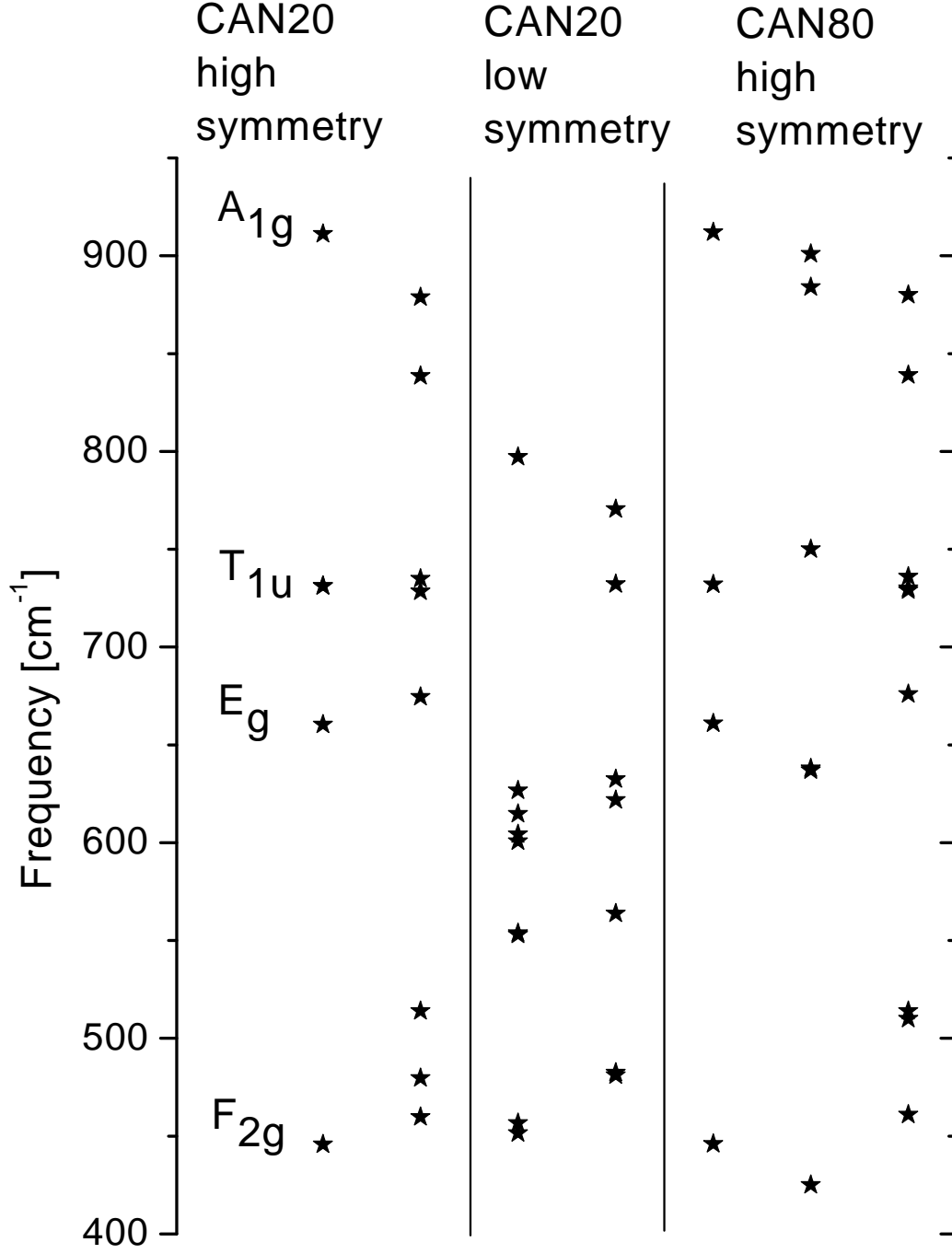


FIG. 4: Results of first principles computations of phonon frequencies in different supercells of CAN: the data for the 20-ion supercell¹⁶ are shown for comparison with our computation for 80-ion supercell of CAN.

TABLE IV: The relative integral intensities obtained in the computation of CAN ($P2_1/n$). The stars show the modes, which are closest to those obtained under the $Fm\bar{3}m$ constraint.

ν [cm^{-1}]	$I_{i }^{powder}$	$I_{i\perp}^{powder}$	I_{it}^{powder}
797*	1.2034	0.0013	1.2048
554*	0.0114	0.0086	0.0200
553*	0.0149	0.0100	0.0249
457*	0.1927	0.1442	0.3368
452*	0.1698	0.1273	0.2971
446*	0.1443	0.1082	0.2526
242*	0.0306	0.0228	0.0534
211*	0.0169	0.0127	0.0296
188*	0.0324	0.0241	0.0565
770	0.0004	0.0003	0.0008
351	0.0015	0.0011	0.0026
732	0.0027	0.0020	0.0047
482	0.0179	0.0134	0.0312
289	0.0000	0.0000	0.0000
331	0.0168	0.0113	0.0281
237	0.0072	0.0054	0.0126
359	0.0113	0.0084	0.0197
564	0.0030	0.0022	0.0052
185	0.0026	0.0019	0.0045
175	0.0161	0.0121	0.0282
136	0.0109	0.0077	0.0186
182	0.0018	0.0014	0.0032
162	0.0063	0.0042	0.0105
339	0.0079	0.0025	0.0104